Thickness Dependence of the Crystalline Structure and Hole Mobility in Thin Films of Low Molecular Weight Poly(3-hexylthiophene)

Siddharth Joshi,[†] Souren Grigorian,[†] Ullrich Pietsch,*[,†] Patrick Pingel,[‡] Achmad Zen,[§] Dieter Neher,[‡] and Ullrich Scherf[||]

*Solid State Physics, University of Siegen, Walter Flex Strasse 3, D-57068, Siegen, Germany; Institute of Physics and Astronomy, University of Potsdam, Karl-Liebknecht-Strasse 24−25, D-14476 Potsdam, Germany; Institute of Materials Research and Engineering, A*STAR, 3 Research Link, Singapore 117602; and Macromolecular Chemistry, University of Wuppertal, Gauss-Str. 20, D-42097 Wuppertal, Germany*

Received December 16, 2007; Revised Manuscript Received June 5, 2008

ABSTRACT: The morphology of thin films at the polymer-to-insulator interface is of great importance for OFET applications. In order to find a relation between the thickness dependence of structural order and the electrical parameters in low molecular weight ($M_w \sim 2.5$ kDa) poly(3-hexylthiophene) (P3HT), we have performed grazing-incidence X-ray diffraction and field effect mobility measurements. The samples were prepared from solutions with different concentrations by spin-coating mainly onto HMDS-pretreated Si/SiO_2 substrates, resulting in film thicknesses that vary between 10 and 200 nm. The X-ray diffraction curves display Bragg peaks of nanocrystallites diluted into an amorphous matrix where the orientational distribution of the crystallites changes significantly as a function of film thickness. The orientation of nanocrystals was found to be random for the thickest films. Reducing the film thickness, we found an increase in the alignment of the stacking direction of molecules along the surface normal. At same time the mean crystal size along the film normal decreases less than the decrease of film thickness. This is interpreted by a preferential pinning of nanocrystals at the film-to-insulator interface when the crystal size becomes in the order of the film thickness, i.e., below 25 nm. The model of pinning effect is supported by temperature-resolved X-ray measurements performed between room temperature and melting temperature. For films thicker than 25 nm the phase transition appears rather continuously with temperature, but it becomes sharp for thinner films. In contrast to X-ray measurements the field effect mobility is found to be constant within the whole investigated range. Our findings give evidence that the charge transport in low molecular weight P3HT is dominated by the ultrathin layer stabilized at the film-to-insulator interface. Despite the very uniform orientation of the crystallites within this layer, the field effect mobility remains low for all thicknesses. This is attributed to the presence of amorphous regions between highly crystalline domains, which ultimately limits the charge transport in the layer plane.

1. Introduction

The performance of organic field effect transistors (OFETs) based on solution-processable polymeric as well as small-molecular semiconductors has impressively improved during recent years.[1,2] These devices have been developed to realize low-cost, large-area electronic products.[1−4] Primarily, highly soluble conjugated polymers are among the most promising materials for OFET devices. Regioregular poly(3-hexylthiophene) RR-P3HT is one of the most studied π-conjugated polymers used in polymer electronics which has demonstrated a high charge carrier mobility in the range of $10^{-2}-1$ $cm^2/(V\,s)$ so far.[5] This can be explained by the highly ordered microphase-separated structure where the densely packed and planarized backbones are separated from more disordered system.

RR-P3HT is one of the important members of the poly(3-alkylthiophene) family, with a rigid conjugated backbone and flexible alkyl side chains, introduced for greater solubility. Already in melt this kind of polymers exhibits microphase separation between the main chain and the alkyl side chains, leading to a layered liquid crystalline structure.[6] Upon crystallization the layered structure is preserved, and the main chains as well as the side chains order onto a common crystalline lattice. It was found that in such a class of material the length and bulkiness of the side chains strongly influence the charge carrier mobility.[7−9] There are several known parameters affecting the morphology of P3HT thin films, mainly the degree of regioregularity, the method of film deposition, annealing, molecular weights, nature of solvent. Until now, various studies have been done on the film structure,[10−12] the molecular weight dependence,[12−14] preparation conditions,[3,5,12] pretreatment of dielectric gate insulator,[5,11,15,16] and solvent used for the film preparation.[3,17] Unfortunately, the relation between structure and electrical properties of films investigated is not clear yet due to the lack of a generally accepted and reproducible receipt of film preparation.

One intriguing property of P3HT is the pronounced dependence of the field effect mobility on molecular weight as first reported by Kline et al. and Zen et al.[13,14] It has been found that low molecular weight samples exhibit a rather low mobility though the layers appear more crystalline than films of high molecular weight P3HT. Kline et al.[18] proposed that in low MW samples charge carriers are trapped at the boundaries between highly crystalline grains, while for high MW material, ordered domains are interconnected by long polymer chains. The interpretation of Zen et al. takes into account that layers from polymers generally exhibit a semicrystalline morphology.[11,14] According to their studies, the crystalline domains in short chain P3HT are separated by amorphous regions formed by chain ends and very short chains, which hinders the motion of charges between ordered areas. Transmission electron microscopy

* To whom correspondence should be addressed. E-mail: pietsch@physik.uni-siegen.de.
[†] University of Siegen.
[§] A*STAR.
[‡] University of Potsdam.
[||] University of Wuppertal.

10.1021/ma702802x CCC: $40.75
Published on Web 08/28/2008

Table 1. Calculated Thickness and Structural Properties of Crystallites of P3HT Samples at Room Temperature

S.N.	sample	thickness t, (nm)	d_{100} (nm)	d_{020} (nm)	crystallite size L_c(nm)
1	40 mg/mL on HMDS	no thickness oscillation found	1.57 ± 0.02	0.38 ± 0.02	40.0 ± 0.5
2	10 mg/mL on HMDS	48 ± 3	1.56 ± 0.05	0.38 ± 0.02	23.5 ± 2
3	5 mg/mL on HMDS	40 ± 3	1.55 ± 0.07	0.38 ± 0.03	24.7 ± 2
4	5 mg/mL on OTS	40 ± 3	1.55 ± 0.07	0.38 ± 0.03	23.1 ± 2
5	3 mg/mL on HMDS	27 ± 2	1.56 ± 0.07	0.38 ± 0.04	16.8 ± 3
6	1 mg/mL on HMDS	10 ± 2	1.55 ± 0.05	0.38 ± 0.05	12.4 ± 3

studies by Brinkmann and Rannou on epitaxially grown thin films of low and high molecular weight P3HT supported the view that the morphology of these layers is semicrystalline, with lamellae of well-ordered chains separated by amorphous interlamellar regions.[19] They further concluded that the higher mobility of long chain P3HT is due to the presence of so-called tie molecules, which interconnect the crystalline lamellae through the amorphous regions. Zhang et al.[20] recently have presented AFM and X-ray data on highly ordered ultrathin layers of P3HT with molecular weight ranging from 2.4 to 18.4 kg/mol. The most characteristic feature of all layers was the presence of nanofibrils, densely packed in a rather periodic fashion. Interestingly, the periodicity was larger than the contour length of the chains, again suggesting that the crystalline nanofibrils made from extended polymers are separated by disordered regions (with an average width of about 6 nm).

Interestingly, Kline et al. recently reported a high mobility of up to 10^{-3} cm^2/(V s) for low molecular weight P3HT casted on octadecyltrichlorosilane (OTS)-treated SiO_2.[18] The same material on SiO_2 treated with hexamethyldisilizane (HMDS) exhibited a mobility of only 10^{-6} cm^2/(V s). On the basis of X-ray rocking curve measurements, the authors demonstrated the existence of highly oriented crystals of P3HT at the buried interface to the SiO_2 gate insulator. They also found that the concentration and orientation of these crystals depended on the kind of SiO_2 surface treatment. The good transport on OTS was explained by the presence of highly oriented crystals at the buried interface, equivalent to only a small number of intergrain boundaries in the plane of charge transport. However, the observation of a high mobility in the low molecular weight P3HT layer seems to be contradictory to the structural model outlined above, in which the crystalline lamellae are separated by amorphous interlamellar regions.

It is well accepted that the first few monolayers close to the gate oxide are mostly responsible for the efficient charge flow from source to drain inside the active channel region.[21] Therefore, it seems to be important to obtain information on the particular film structure close to the interface of the gate insulator. Unfortunately, the recent studies on low molecular weight P3HT did not provide sufficient information on the effect of layer thickness on morphology and mobility. Jia et al.[22] have shown the thickness effect on the performance of high molecular weight P3HT-based (98.5% regioregular) OFET devices. They found that the mobility and the drain current increase with thickness. The on−off ratio decreases and saturates for thicknesses above 60 nm. As these observations are purely based on device characteristics, they cannot give a clear hint on the thickness-dependent structural order variation inside the individual films. Therefore, a systematic study of the crystalline structure as a function of film thickness in P3HT is still desirable.

In this paper we present X-ray investigations of the structure and its thermal behavior of low molecular weight P3HT films in relation to charge carrier mobility measured at respective thin film OFETs. At first glance our work is focused on systematic study of structural and electrical properties of the films as a function of film thickness for mainly HMDS-treated SiO_2 insulator surfaces.We will show that a high crystalline order as found for thin films does not result in a higher carrier mobility as long as the nanocrystals are separated by large amorphous regions.

2. Experimental Section

RR-P3HTs were prepared by the Grignard metathesis procedure according to McCullough and co-workers.[23] The raw polymer was fractioned by applying the solvent-extraction method[24] using ethyl acetate as a solvent. The procedure yielded a first, low molecular weight polymer fraction of 3.5 kDa with a polydispersity index of 1.4. The EA fraction mainly contains short-chain oligothiophenes. Unreacted monomers and leftover catalyst have been removed during the work-up of the reaction mixture (by careful washing with aqueous EDTA/water and solvent extraction with methanol). The main termination reaction is a debromination of the 2-bromothienyl end groups of the growing P3HT chains, leading to short-chain oligothiophenes. Layers for structural studies and for mobility measurements were prepared on n-doped Si covered with 300 nm thick thermally grown SiO_2. After cleaning, the SiO_2 surface was passivated by a combined oxygen plasma treatment and silanization using hexamethyldisilazane (HMDS)[5,11] to passivate the SiO_2 surface such that the charge carrier mobility in the P3HT thin films is enhanced.[25] In one case (sample 4) the surface was alternatively treated with octadecyltrochlorosilane (OTS). To vary the thickness of the polymer layer, the concentration of P3HT in chloroform solution was varied, keeping the other conditions (spinning speed 1200 rpm and spinning time 60 s) constant (see Table 1).

For OFET devices, a 100 nm thick interdigitating gold structure was evaporated on top of the polymer layer, acting as source and drain electrodes with a channel length of 0.1 mm and a channel width of 148.5 mm. For technical reasons the thickness of the active polymer layer in the OFET devices was measured using a DEKTAK3 surface profiler. The reported film thicknesses are mean values from six measurements at different positions at the surface of one sample. Note that thickness measurements with a surface profiler generally underestimate the polymer layer thickness, especially when studying soft polymers as those used in this study. In average the thickness values measured by X-rays were about twice as large as those obtained using the surface profiler.

Electrical characterization of the OFET devices was performed using an Agilent 4155C semiconductor parameter analyzer. The output characteristics were measured in a cyclic procedure. The field effect mobility μ_{sat} was extracted from output characteristics and calculated from the saturation region, according to the following equation:

$$I_{sat} = \frac{WC_i}{2L}\mu_{sat}(V_{GS} - V_T)^2 \quad (1)$$

where C_i is the capacitance per unit area (11.9 nF/cm^2) of the gate dielectric, V_T is the threshold voltage, and W and L are the channel width and length, respectively. All OFET characterization and preparation steps were executed in an inert N_2 atmosphere.

The X-ray grazing incidence diffraction measurements were performed at the German 1.5 GeV storage ring DELTA located at Dortmund university using a wavelength of $\lambda = 0.112$ nm and at the undulator beamline ID10B of European Synchrotron Research Facility (ESRF), Grenoble, France, running at 6 GeV ($\lambda = 0.0924$ nm). We used a point detector at DELTA and a 1D position-sensitive detector (PSD) oriented parallel to the surface normal at ESRF. In addition, we took 2D pictures using an image plate at DELTA ($\lambda = 0.0814$ nm). Whereas the beam size at DELTA was

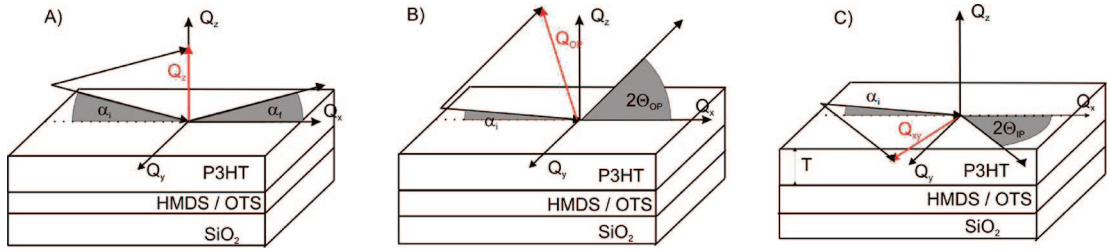

Figure 1. X-ray scattering geometries used.

0.5×1.5 mm^2 (vertical $\times$ horizontal), at ESRF the beam size was as small as 0.1×0.5 mm^2 and a soller slit in front of the detector provided an in-plane angular resolution of $\Delta\theta = 0.1°$. In combination with the much higher incident intensity and the much lower scattering background, the experiment at ESRF provided at least 2 orders of magnitude higher peak-to-background ratio compared to the experiment at DELTA.

The setups for X-ray diffraction measurements are shown in Figure 1. The film thickness can be measured precisely by X-ray reflectivity setup (Figure 1a). Here, the angles of incidence, α_i, and exit angle, α_f, vary by the same amount resulting in a momentum transfer Q_z, parallel to the surface normal. When α_i is equal to or smaller than the critical angle of total external reflection α_c, the incident X-rays undergo total external reflection and penetrate into the sample as evanescent waves which limits the penetration depth of the probing X-ray beam into the sample to a few nanometers only.[26] The α_c value is given by

$$\alpha_c = (\lambda^2 r_e N/\pi)^{1/2} \quad (2)$$

where r_e is classical electron radius and N is electron density per unit volume of material. For films with a thickness of a few nanometers, the reflectivity scans cannot be extended to angles much above α_c because the penetration depth rises rapidly to several microns considering the low absorption coefficient of organic material. However, keeping $\alpha_i < \alpha_c$, the evanescent wave can be exploited to enhance the scattering intensity of the thin films (grazing-incidence diffraction): Optimum conditions are achieved if α_i is fixed above the critical angle, α_{cf}, of the P3HT thin films but below the critical angle of the substrate, α_{cs}.[26] Considering the wavelengths used for line scan measurements at DELTA and the ESRF, the critical angles of the thin polymer films are $\alpha_{cf} = 0.12°$ and 0.09°, respectively, which compares to those of the underlying silicon substrate $\alpha_{cs} = 0.16°$ and 0.133°. For the X-ray image plate measurements these values are $\alpha_{cf} = 0.08°$ and $\alpha_{cs} = 0.12°$, respectively. Using grazing-incidence out-of-plane diffraction (GOD), α_i was fixed at the condition $\alpha_{cf} < \alpha_i < \alpha_{cs}$. The grazing-incidence angle keeps fixed, and the detector angle $\alpha_f \approx 2\Theta_{OP}$ is scanned in a wide angular range (Figure 1b). Subsequently, the scattering vector **Q** is not directed along the surface normal. Bragg peaks appear whenever the material shows a wide distribution of crystal orientations. Finally, grazing-incidence in-plane diffraction (GID) is performed at same conditions for α_i, but the scattering signals were collected by changing the in-plane $2\theta_{in} = \theta_i + \theta_f$ angle of the detector (Figure 1c). In GID all diffraction vectors are laying in the surface plane. In reciprocal space coordinates, the momentum transfers can be expressed by the following relations with the scattering angles:

$$Q_z = (2\pi/\lambda)(\sin\alpha_i + \sin\alpha_f) = (4\pi/\lambda)\sin\alpha_i, \quad \text{for reflectivity scans}$$

$$Q = (2\pi/\lambda)(\sin\alpha_i + \sin\alpha_f) \approx (2\pi/\lambda)(\sin 2\Theta_{op}), \quad \text{for GOD, at small } \theta_{OP}$$

$$Q_{x-y} = (2\pi/\lambda)(\sin\theta_i + \sin\theta_f) \approx (2\pi/\lambda)(\sin 2\Theta_{in}), \quad \text{for GID scans} \quad (3)$$

All X-ray measurements were performed under vacuum conditions ($\sim 10^{-3}$ mbar) using the DHS 900 domed hot stage provided by Anton Paar GmbH, Graz, Austria. This was essential in order to avoid substantial radiation damage at the polymer sample and to reduce background scattering. For temperature-resolved measurements the temperature has been increased in steps of 10 °C from room temperature to the melting point of the individual sample with an accuracy of ±0.5°. Data were taken after stabilization of the respective temperature at the sample surface.

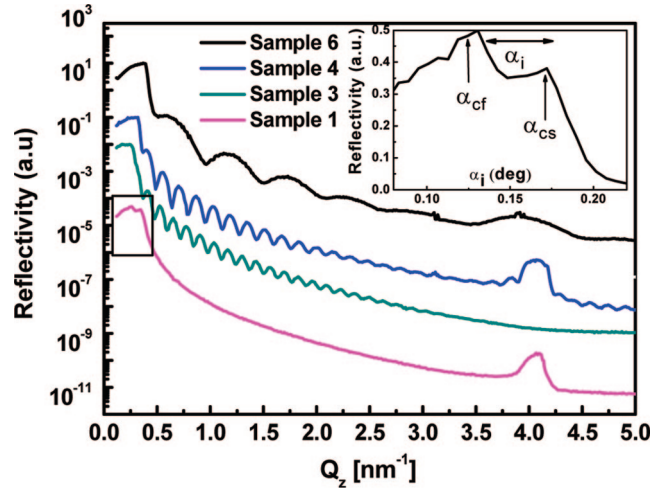

Figure 2. Reflectivity measurements of P3HT samples of various thicknesses. The inset shows the angular region of total external reflection of sample 1. Further GID and GOD scans were recorded setting the incidence angle α_i to $\alpha_{cf} < \alpha_i < \alpha_{cs}$, where α_{cf} and α_{cs} are the angles of total external reflection of film and substrate, respectively.

3. Results

3.1. Structure Investigation at Room Temperature. The structure of P3HT films prepared on HMDS- and OTS-treated SiO_2 substrates were analyzed by X-ray reflectivity, 2D image plate exposures, and GOD and GID line scans. All the samples analyzed in this study are summarized in Table 1.

Determination of Layer Thickness. Reflectivity measurements were performed to determine the film thicknesses. Figure 2 shows the results of the reflectivity measurements of the samples prepared from different solution concentrations. Because of interference of waves reflected from the vacuum−sample and film−substrate interfaces, Kiessig fringes are clearly visible. The film thickness, t, was obtained from the distance ΔQ_z between two consecutive maxima, where $t = 2\pi/\Delta Q_z$. Except for the thickest sample 1, all samples show a large number of Kiessig fringes which verify the homogenity of the film thickness, which fluctuates by only about 3 nm within the illuminated sample area. The extracted film thickness values are shown in Table 1. Considering the relation between concentration and film thickness of the other samples, the thickness of sample 1 was estimated to be $t \approx 200$ nm. Because of the large thickness, sample 1 displays the two critical angles, α_{cf} and α_{cs}, very well (see inset of Figure 2). In the following the incidence angle, α_i,

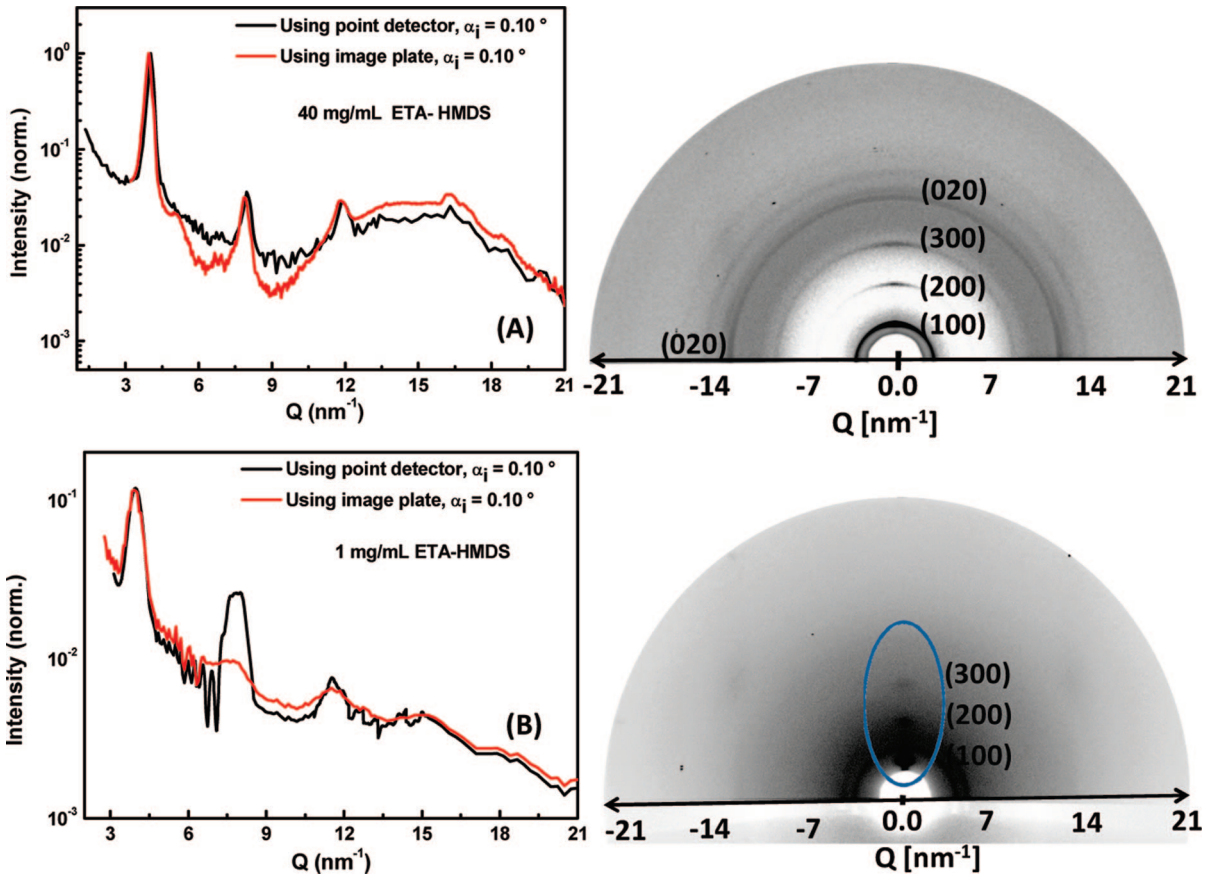

Figure 3. 2D images taken in grazing-incidence geometry of sample 1 (A) and sample 6 (B) at 15.2 keV (right). Extracted line scans are compared with point detector measurements taken at equal scattering geometry (left).

was fixed $\alpha_{cf} < \alpha_i, < \alpha_{cs}$, for both GOD and GID scans in order maximize ratio between film to substrate scattering.

The reflectivity scans can be extended up to the first Bragg peak indexed by (100). Here the intensity has already dropped by at least 6 orders of magnitude. However, the 100 peak appears for all samples except sample 3. Using Scherrer's equation[27] (see later), the measured FWHM of the 100 peak was used to determine the correlation length, L_c, parallel to surface normal. L_c can be identified as the crystallite size in this direction and is listed in Table 1. L_c for sample 3 was determined from GOD scans (see below).

Structure Investigation. Prior to GID and GOD line scans we have probed the thickest (sample 1) and thinnest sample (sample 6) by image plate exposures. Here $\alpha_i < \alpha_{cs}$ was fixed, and the 2D scattering of the film was recorded within 30 min of exposure time. For sample 1 we find closed rings with **Q** radii corresponding to (100) and its higher multiples with a small preference along the surface normal. In addition, one finds a ring related to (020) (Figure 3a). The peaks appear onto a nonuniform background caused by diffuse scattering from disordered P3HT, the SiO_2, and the background scattering of the experiment. As the background intensity is low close by the 200, no closed ring is seen for this reflection. However, a line scan extracted from image plate data show the (*h*00) and (020) peaks which coincide well with a scan taken with a point detector under same geometric conditions.

In contrast to this, sample 6 displays distinct scattering spots in out-of plane direction (Figure 3b) without a remarkable ring structure. Also, there is no indication for the (020) peak. The different structural behavior found in both images can be interpreted by the transition from a random to a preferential orientation of the crystallites as a function of film thickness.

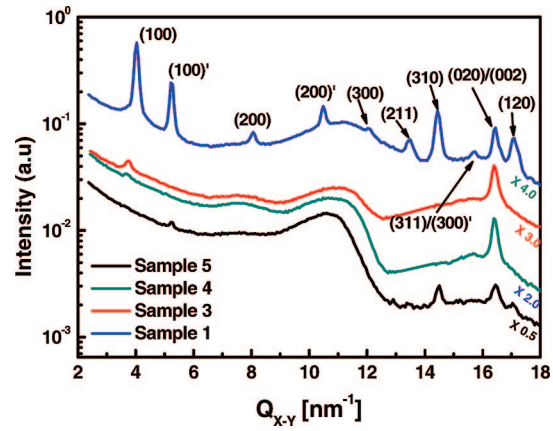

Figure 4. GID scans from samples with different thickness measured at $\alpha_i \leq \alpha_{cs}$. For better clarity all scans are separated by an offset factor.

In order to study this transition in detail, we performed GOD and GID line scan measurements with much higher intensity of the incident beam and improved signal-to-noise ratio at ESRF. Figure 4 shows the GID (in-plane) scans of films with four different thicknesses and two different surface treatments. At least 11 sharp reflections are visible in the case of the thickest sample 1 as already seen on the image plate picture in Figure 3a but at least a few peaks in the high angle range for the other samples. Following previous structure investigations at same material,[5,13,14] the low angle peaks (100), (200), and (300) are related to the lamellar ordering of the phase separated structure in direction of the alkyl side chains. Further peaks appear at $Q_{xy} = 13.5$, 14.4, 15.7, 16.4, and 17.0 nm^{-1}. The peak at $Q_{xy} = 16.4$ nm^{-1} is indexed by (020)[5,11,18] and is associated by the

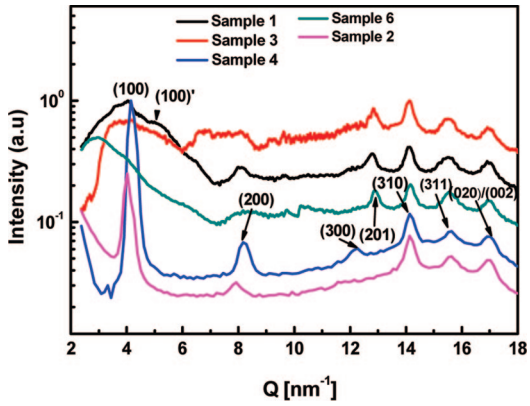

Figure 5. GOD scans for samples of different thicknesses. The incidence angle is $\alpha_i \leq \alpha_{cs}$. In low angle range the diffraction curves suffers from parasitic scattering of beamline components. For information in this Q range refer to Figure 3.

in-plane $\pi-\pi$ stacking distance, which is 0.388 nm. Following the structure solution of Prosa et al.[10] and Brinkmann et al.,[19] this distance is very close to the distance between the two sulfur atoms of the thiophene backbones of 0.38 nm indexed with (002). Both peaks can not be exactly resolved in our experiment. The other peaks are located on a broad amorphous background. One is centered at 11.0 nm^{-1} and is less dependent on film thickness; the second amorphous halo is centered at 16.0 nm^{-1} and is addressed to the amorphous scattering of SiO_2. It is observed that the low angle peaks decrease as the film thickness decreases. One can observe the decrease of (100) peak intensity of sample 3 (t = 40 nm) in comparison to sample 1, and it completely disappeared for sample 6 (t = 10 nm). This behavior is same for HMDS- and OTS-treated samples of same thickness (compare samples 3 and 4). At the same time most of the other wide angle peaks disappear with decreasing film thickness as well except that of (020/002). Therefore, the vanishing peaks must be indexed by reflections with $h \neq 0$. The samples with the intermediate thicknesses acquiesce into the trend (data not shown). Figure 4 also shows the existence of two sets of additional reflections for the thickest sample, which is a direct evidence of polymorphism. The second form indexed with (100)′ appears at higher Q_{x-y} = 5.25 nm^{-1} compared to (100) (Q_{x-y} = 4.05 nm^{-1}). It reflects an interplanar distance of d = 1.20 nm compared to the main form with d = 1.56 nm. The appearance of higher order peaks such as (200)′ and (300)′ in addition to (200) and (300) gives evidence for perfect ordering of both polymorphs. Interestingly, such dual form is only observed at samples with highest concentration but not for thinner films. Like for thick films, polymorphism was also found for powder samples.[11]

Figure 5 shows the GOD scans taken at ESRF. Unfortunately, by technical reasons the low angle peaks in the range Q < 8.0 nm^{-1} of samples 1, 3, and 6 are affected by parasitic scattering from beamline components. These deficits can be compensated by GOD line scans for sample 1 (after thermal treatment) and sample 6 shown in Figure 3a,b where most of the high order peaks are no more visible due to the much lower peak to noise ratio. Considering the curves in Figures 3a,b and 5, most of the wide angle peaks already found in GID (Figure 4) appear for the thickest sample (sample 1). In addition, further peaks are displayed at Q_{xy} = 12.8, 14.4, 15.7, and 17.0 nm^{-1} where the second one is most intense. These peaks are sitting on an amorphous halo centered at Q_{xy} = 13.5 nm^{-1}, which approximately scales with film thickness and may reflect the diffuse scattering from disordered polymer units. As found in GID films of same thickness but prepared on HMDS- or OTS-treated substrates (sample 3 and 4) display same number of peaks with nearly same intensities. In contrast to GID, the low order Bragg peaks appear for all samples independent from film thickness. This finding is in agreement with the image plate data shown in Figure 3. As long as the nanocrystallites are randomly oriented, the scattering provides closed Scherrer rings (Figure 3a) and distinct low angle peaks are visible in GID (Figure 4) and GOD (Figure 5). Reducing the film thickness the low angle peaks in GID disappear but remain in GOD, which is the situation shown in Figure 3b. However, there is a discrepancy in explaining the wide angle peaks missing in Figure 3b but being clearly visible in Figures 4 and 5. This discrepancy can be explained by the different sensitivity of DELTA and ESRF experiments. The orientation distribution of nanocrystals contains two components; one is the preferential alignment of nanocrystals along the surface normal, and the second is associated with the remaining, not aligned, nanocrystals. The ratio of both components is changing with decreasing the film thickness for the benefit of the aligned component. Because of the higher background scattering at DELTA experiment, the random component is no more visible in Figure 3b but measurable in Figures 4 and 5 taken at ESRF. On the basis of present data, we cannot decide whether the nonaligned component of orientation distribution is in fact random or perhaps bimodal, one is corresponding to edge-on and another to face-on orientation of crystallites with respect to the interface.

On the basis of data shown in Figures 4 and 5, we have calculated the interplanar distances, d_{100} and d_{020}, and the size of crystals, L_c, and summarized in Table 1. d_{100} and d_{020} remain constant in all scan directions and for all thicknesses within error bars. However, the present d_{100} values are smaller than that obtained from our previous powder measurements (d_{100} = 1.58 nm).[14] Using Scherrer formula,[27] we have computed the average size of crystals for the samples of different thickness. Using the width of the (100) peaks, the crystal size in that direction varies from 12 nm for sample 6 to 40 nm for the thickest film (sample 1).

Structure Model. Using all angular positions of peaks measured in GOD and GID scans, we evaluated an average unit cell of the nanocrystallites present within P3HT samples. For sample 1 we have found a larger number of peaks in both GOD and GID scans. For thinner films most of the peaks are still visible in GOD, but only one or two of the wide angle peaks remain in GID. This refers to a crystal structure of perfect crystallites which represents the particular low molecular weight fraction under investigation. The peak positions found do not match with the assumption of an orthorhombic cell as suggested by Tashiro et al.,[28] with a = 1.663 nm, b = 0.775 nm, and c = 0.777 nm. Multiples of (100) and one of both (020) and (002) were found by Kline et al.[12] only. Our experiment cannot be indexed by an orthorhombic cell. However, the number of structure peaks is still too small in order to find a unique structure solution. Our fits have considered the known $\pi-\pi$ distance of $b/2$ = 0.38 nm. However, the unit cell can be triclinic or monoclinic. In present case several unit cells match to the experimental data. Out of them we have used the unit cells with parameters a = 1.59 ± 0.02 nm, b = 0.75 ± 0.02 nm, c = 0.76 ± 0.02 nm, β = 101 ± 3°, and $\alpha \approx \gamma \approx 90°$ for further indexing. This cell is approximately monoclinic and not much different from the structure solution suggested by Brinkmann et al.[19] and Prosa et al.[29] and which were extracted from material which differs from the low molecular weight fraction probed here. Based on this, our model corresponds to structure type I. A schematic scheme of the unit cell is shown in Figure 6. Because the lattice parameters b and c are approximately same the peaks indexed with (020) and (002) may merge together. Because we are rather interested to investigate how the structure

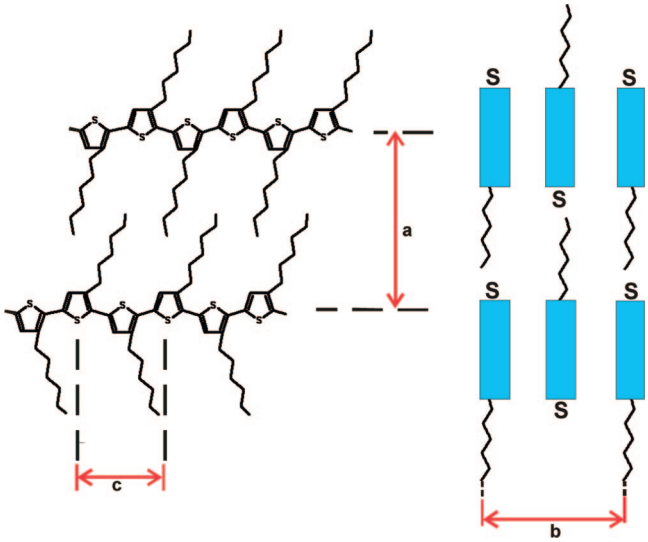

Figure 6. Sketch of the proposed monoclinic unit cell of crystallites in LMW P3HT.

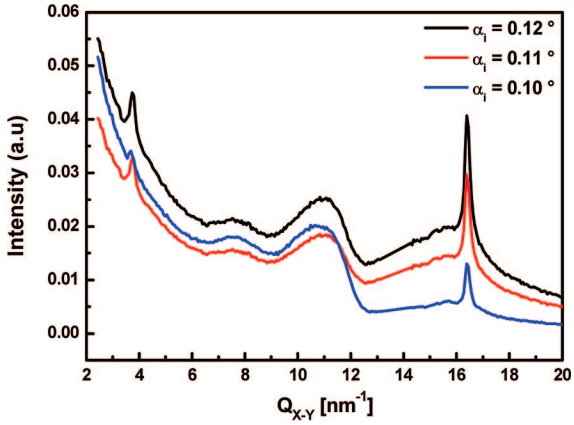

Figure 7. In-plane measurements of sample 3 at three different α_i, corresponding to a probe of the surface and the whole film.

parameters change with film thickness, we were not keen to find the best structure solution.

Interface Induced Ordering. Figure 7 shows the GID scan of sample 3 taken at three different angles of incidence, changing from $\alpha_i = 0.10°$ to 0.12°, where $\alpha_i \leq \alpha_{cs}$. Whereas in the first case X-rays penetrate the top region of the film only, the other cases probe the whole film. Two peaks are visible, (100) and (020), increasing in intensity for increasing α_i. At same time the intensity of the amorphous halo around $Q_{xy} = 16.0$ nm^{-1} increases as well, which is identified by scattering from SiO_2. Similarly, the halo present at $Q_{xy} = 11.0$ nm^{-1} is not affected. Both give evidence that the crystal peaks are mainly caused by crystallites located at the film to insulator interface and the in-plane ordering maintained throughout the film thickness.

3.2. Structure Investigation as a Function of Temperature. *Temperature Treatment*. Except for high molecular weight observed by Werzer et al.,[30] P3HT films were not systematically inspected at varied temperatures above room temperature. However, technically most of the films were treated by an annealing step to improve the film quality.[11,14] Figure 8 shows the GID scans of sample 1 before and after heating above 100 °C. The mentioned dual form is only present in the pristine sample at room temperature. After a heating cycle the structure with $d_{100} = 1.20$ nm disappeared, indicating that the second polymorph form is thermodynamically less stable compared with

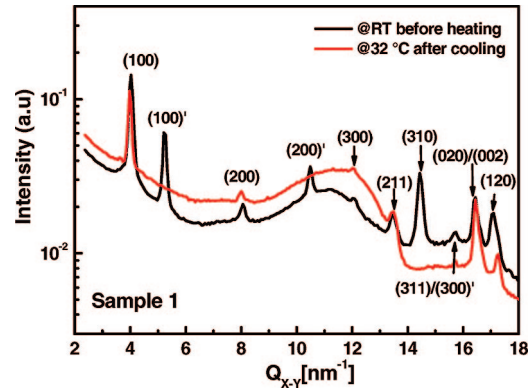

Figure 8. Temperature-dependent study of sample 1 at $\alpha_i \leq \alpha_{cs}$. The polymorphism of the pristine sample disappears after the heating cycle.

the first one with $d_{100} = 1.56$ nm. At the same time the peak at $Q_{xy} = 14.4$ nm^{-1} disappeared accompanied by a change in the intensity ratio of both amorphous halos. Except a change in intensity of background scattering, all other crystals peaks are not affected. This indicates that the crystal structure is maintained after annealing.

Thermal Expansion. Parts A and B of Figure 9 show the temperature dependence of both (100) and (020) reflections measured for sample 1 in GOD and GID, respectively. From Figure 9A one can see that as the temperature increases, the (100) reflection shifts to lower Q values accompanied by a decrease of peak intensity. This trend is continuous up to the complete disappearance of the peak. The temperature of complete disappearance can be associated with the melting point of the ethyl acetate fraction of P3HT. Prior to melting, the d_{100} increases with increasing temperature, indicating expansion of distance of the alkyl stacking. At the same time, the (020) peak positions are shifting toward higher Q_{xy} values as the temperature increases, indicating a decreasing d_{020}, i.e., a reduction of the distance (Figure 9B). Combined, an increase of temperature gives rise to an expansion of the nanocrystals along the axis of alkyl chains (**a** direction) accompanied by a contraction of $\pi-\pi$ distance (**b** direction). After cooling down the lattice deformation is almost reversed.

Influence of Film−Substrate Interaction. Figure 10A shows the temperature variation of the (100) peak intensity measured by GOD at four samples of different thickness measured at ESRF. It shows a continuous decrease in intensity vs temperature for sample 1 and 3 but a nearly constant intensity for the thinner sample 5 ($t = 27$ nm) up to about 75 °C followed by a sharp drop. The same behavior was found for another sample similar to sample 6 of this series but at a different experiment performed at DELTA. This much thinner sample ($t = 10$ nm) exhibits a sharp drop of (100) intensity at 70 °C. This behavior can be interpreted by a strong substrate−layer interaction becoming remarkable at thin films only. The interaction also modifies the character of phase transition. It appears continuous decrease of intensity for thick films but sharp decrease of intensity for thin films. This can be explained by the interaction energy between the nanocrystals pinned at the insulator interface. In thick films crystal melting may start at the film surface and proceed down to the interface of the film where the interactions are stronger and thus the melting temperature higher, as found for systems with interface melting.[31] This behavior differs from thin layers with a sharp melting temperature. To understand further features of the thermal expansion, we have plotted the interplanar distance d_{100} vs temperature. As seen in Figure 10B, both thin and thicker films show the same increase of d_{100} between room temperature and about 80 °C but with rather large error bars.

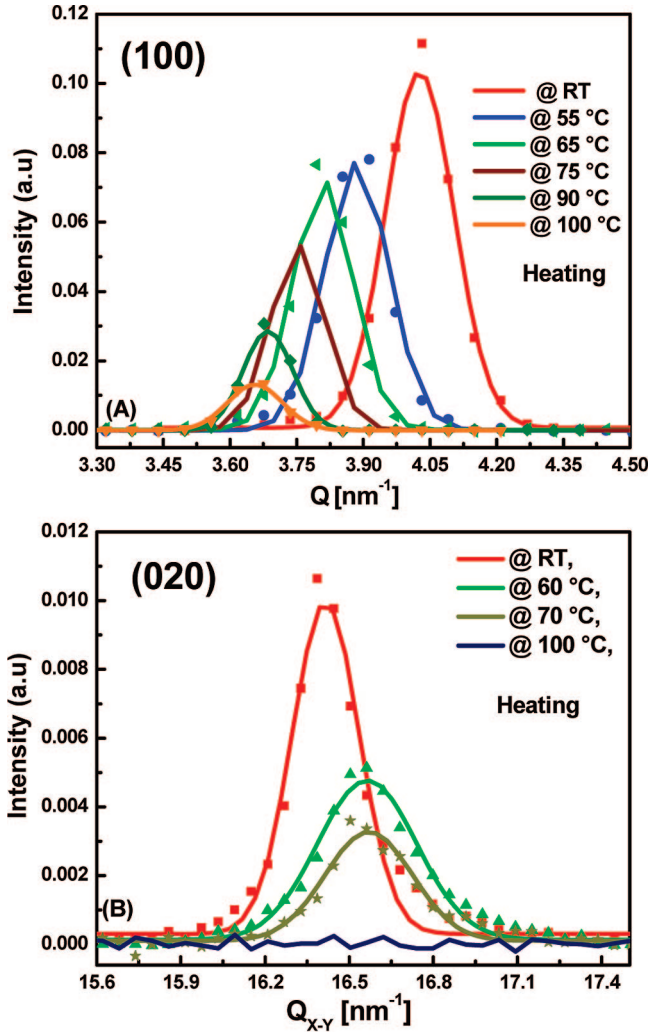

Figure 9. (A) Temperature dependence of the (100) peak studied for sample 1 at $\alpha_i \leq \alpha_{cs}$. The shift of the peak toward lower Q_{x-y} indicates the increase of d spacing along normal direction. (B) Temperature dependence of (020) peak studied at sample 3 at $\alpha_i \leq \alpha_{cs}$. The shift of (020) peak toward higher Q_{x-y} value indicate the decrease of d spacing lateral direction.

Presently we are not able to answer the question whether or not there is a vertical temperature gradient in lattice parameters 'a'.

3.3. Mobility Measurements. Field effect mobility measurements have been performed for samples with different thickness to correlate the structural parameters with electrical properties. The corresponding output and transfer characteristics display a remarkable hysteresis. Linear and saturation regions are quite blurred and unstable. To minimize these hysteresis effects, we have averaged the forward and backward scans of the output characteristics for every gate bias. OFET mobilities as calculated from the gate-bias dependence of the averaged saturation current are plotted in Figure 11.

Except for the thinnest film, the field effect mobility remains almost constant within the wide range of thicknesses, with an average mobility of ca. 10^{-6} cm^2/(V s). Fluctuations within 20% can be a related to varying experimental conditions. Particular AFM inspections at the thinnest film gave hint for incomplete wetting which might be the reason for the much lower field effect mobility of this sample compared to the others. When comparing the results from X-ray and OFET thickness-dependent measurements, one should keep in mind that the thickness determination with a surface profiler (as used to determine the polymer layer thickness in the transistor structures) underestimates the true thickness. For thin layers, the thickness values measured with the profiler are approximately half of those obtained from the analysis of the Kiessig fringes. This can be explained by the compression of the soft polymer by the probe of the profiler.

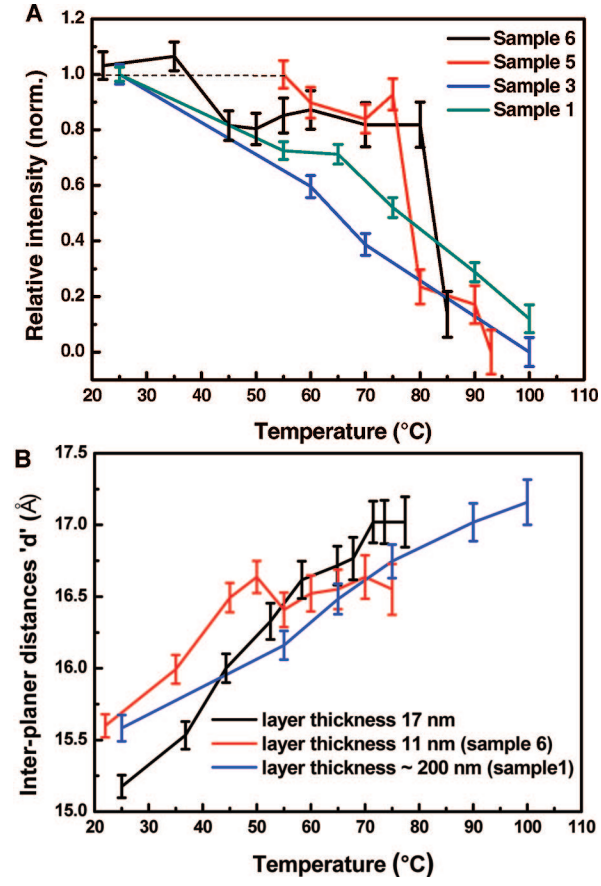

Figure 10. (A) Temperature-dependent relative intensity studies of thick and thin films measured at ESRF. The sample shown in black was measured at DELTA. (B) Temperature-dependent inter-planar distances 'd' of three samples with different thickness.

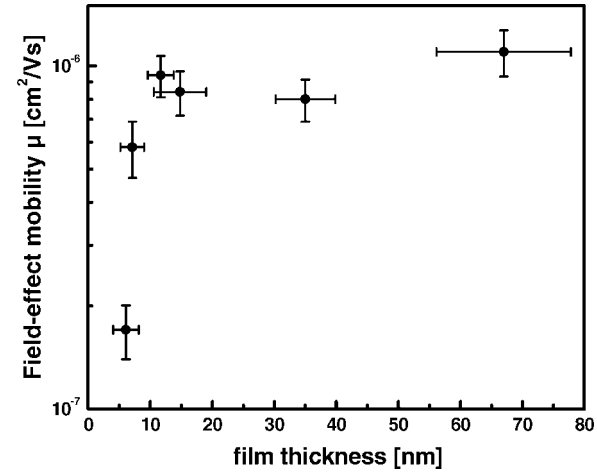

Figure 11. Thickness-dependent field effect mobility of low molecular weight P3HT, extracted from the OFET output characteristics (I_{DS} vs V_{DS} at fixed V_{GS}).

We further observed that the field effect mobility increases by a factor of 2 by annealing the polymer layer (before deposition of the source and drain contacts) for 5 min at 55 °C, as compared to the pristine device, which was left in a vacuum for 5 h to remove residual solvent from the film. While the

pristine sample has a field effect mobility of $(4.1 \pm 0.6) \times 10^{-7}$ $cm^2/(V\ s)$ (film thickness 18.3 ± 1.6 nm as determined with a surface profiler) the mobility of the annealed sample was $(9.5 \pm 1.3) \times 10^{-7}$ $cm^2/(V\ s)$ (for a comparable film thickness of 23.5 ± 2.4 nm).

4. Discussion

We have shown that the crystalline order of films made of P3HT changes as a function of film thickness. For films with thicknesses in the order of few 100 nm the film structure consists of randomly oriented nanocrystallites diluted in an amorphous matrix (see Figure 3a). Decreasing the film thickness, the main change of morphology consists in narrowing the distribution of crystal orientation (Figure 3b). Following the suggestion by Kline et al.,[18] this is explained by a preferential alignment of crystals at the film-to-insulator interface. Kline et al.[18] verified their assumption by the very narrow width of (100) rocking curves for thin films. We found evidence by at least three different experiments: using α_i-resolved measurements, we have shown that the crystal peak intensities and the scattering from the interface increase with penetration depth of probing X-ray with the sample independent from whether the film was prepared either on HMDS- or OTS-treated substrates. In addition, we have shown that the melting behavior of the films changes qualitatively by decreasing the film thickness. Finally, we found direct pictures of the changing orientation distribution by imaging of 2D scattering. Moreover, using highly intense synchrotron radiation at ESRF, we could determine the orientation of the pinned nanocrystals. For films below about 25 nm we find a drop of (100) peak intensity in GID which is not observed in GOD. The disappearance of (100) peaks in GID can be interpreted by a preferential alignment of the *a*-axis of nanocrystals parallel to the film normal which corresponds to an "edge-on" geometry. Considering the average crystal size as listed in Table 1, the change in alignment appears when the domain size equals to the film thickness. The effect of interface alignment is known from liquid crystals[32] and decays exponentially from the interface toward the bulk. It might be essential for polymers at interfaces as well. The particular control of the interface potential could help for a better understanding of the thickness dependence of mobility.

Regarding the comparison of electronic and structural properties, we found that the mobility remains constant over a wide range of thicknesses, despite a significant increase in in-plane ordering when decreasing the layer thickness, as revealed by our X-ray measurements. On the basis of our structural and electrical properties, we presume the existence of an interface near ultrathin crystalline layer, stabilized by the strong interaction between the polymer chains and the gate insulator, with the main chains oriented almost exclusively parallel to the substrate. This interface region is present in all samples but dominates for samples with thickness below about 25 nm, and it is responsible for charge transport in the OFET measurements. Despite this high structural order, the mobility of carriers remains quite low. As pointed out in the Introduction, several authors provided evidence for the existence of amorphous regions in between highly crystalline lamellae (or nanofibrils) in short chain P3HT samples, even in films grown by epitaxial solidification. It is, therefore, plausible to propose that such interlamellar zones also exist in those highly ordered ultrathin layers stabilized very close to the gate insulator and that they ultimately determine the charge transport in OFETs made from low MW P3HT.

At the moment we cannot provide a conclusive interpretation of the drop in mobility when decreasing the layer thickness further (see Figure 11). Although these very thin layers are characterized by a high degree of chain alignment, with low degree of orientation disorder, one plausible interpretation is that the P3HT film partially dewets below a critical layer thickness.

We did not observe any significant effect of SiO_2 surface treatment on the layer morphology, nor on the transport properties of our low molecular weight material. The carrier mobilities reported here are much lower than those published by Kline et al.[18] for short chain P3HT on OTS, though our X-ray measurements reveal a high structural order of the layer stabilized at the semiconductor−insulator interface. To solve this obvious discrepancy, a comparative investigation of the polymer samples used by them and us would be needed (which is beyond the scope of this paper), but we like to point out again that the low mobility measured in this study is in accordance with the generally accepted structural model for short chain P3HT, as outlined above.

Our X-ray studies on as-prepared layers show the presence of a second metastable polymorph (phase II), which disappears upon annealing. The concurrent increase in mobility of annealed samples suggests that the mobility of carriers in this metastable phase II is quite lower. This lower mobility is probably due to a larger in-plane $\pi-\pi$ stacking distance of polythiophene layers and a lower rate for interchain hopping.

Finally, one has to note that the ESRF measurements have provided a better understanding of structural order in thin films of low molecular weight P3HT. In terms of ordering, we found two components: one aligned and another random in orientation. In terms of crystal structure the larger number of Bragg peaks, in principle, would allow a better structure solution. However, the number of peaks found is still too small for a unique structure solution which holds for most of the structures published in literature. Structure solution of P3HT powders[14,28] provided (100) and (020) peaks which were indexed using respective stereochemical arguments from powder data published by Tashiro,[28] Prosa,[10,29] and Meille.[33] The similar structure solution for low molecular weight P3HT was published by Brinkmann et al.[19] recently. Unfortunately, it cannot be transferred to our material due to the film formation from a different solvent and slightly larger molecular weight of the P3HT that was used in their study. The refined crystal structure is assumed to be an average over the whole sample. The lattice parameters might slightly vary among the crystals and probably change at the film−substrate interface. The latter one could explain that a few peaks appeared in GID or GOD only. This is supported by the polymorphism which appeared at thick pristine films only. It reflects the effect of small fluctuation of crystal growth energy during the preparation process.

We found a complete change of crystal unit cell with increasing temperature. Moreover, the phase transition between solid and melt changes as a function of thickness. It is found to be continuous drop of intensity for thick films but a sharp drop for thinner films. The layer thickness where we found a change in the temperature behavior first gives a rough estimate for the decay length of interface interaction toward the bulk. Because the peaks width remains constant while decreasing in intensity, the numbers of crystallites decrease with increasing temperature for film thickness above the interface decay length. This differs from thin films where the crystals kept pinned at the film−substrate interface up to the melting temperature. Because of the interface interaction, the latter one is expected to change as a function of film thickness.

Acknowledgment. We thank ID10B beamline staff at the ESRF and beamline BL9 staff at Delta for their valuable help. This work was financially supported by the German Science Foundation, the

Fond der Chemischen Industrie, and the Ministerium für Wissenschaft, Forschung and Kultur of Brandenburg.

References and Notes

(1) Dimitrakopoulos, C. D.; Mascaro, D. J. *IBM J. Res. Dev.* **2001**, *45*, 11–27.
(2) Fix, W.; Ullmann, A.; Ficker, J.; Clemens, W. *Appl. Phys. Lett.* **2002**, *81*, 1735–737.
(3) Bao, Z.; Dodabalapur, A.; Lovinger, A. J. *Appl. Phys. Lett.* **1996**, *69*, 4108–4110.
(4) Sirringhaus, H.; Tessler, N.; Friend, R. H. *Science* **1998**, *280*, 1741–1744.
(5) Sirringhaus, H.; Brown, P. J.; Friend, R. H.; Nielsen, M. M.; Bechgaard, K.; Langeveld-Voss, B. M. W.; Spiering, A. J. H.; Janssen, R. A. J.; Meijer, E. W.; Herwig, P. T.; de Leeuw, D. M. *Nature (London)* **1999**, *401*, 685–688.
(6) Ballauff, M. *Angew. Chem., Int. Ed. Engl.* **1989**, *28*, 253–267.
(7) Gartstein, Y. N.; Conwell, E. M. *Chem. Phys. Lett.* **1995**, *245*, 351–358.
(8) Dunlap, D. H.; Parris, P. E.; Kenkre, V. M. *Phys. Rev. Lett.* **1996**, *77*, 542–545.
(9) Novikov, S. V.; Dunlap, D. H.; Kenkre, V. M.; Parris, P. E.; Vannikov, A. V. *Phys. Rev. Lett.* **1998**, *81*, 4472–4475.
(10) Prosa, T. J.; Winokur, M. J.; Moulton, J.; Smith, P.; Heeger, A. J. *Macromolecules* **1992**, *25*, 4364–4372.
(11) Zen, A.; Saphiannikova, M.; Neher, D.; Grenzer, J.; Grigorian, S.; Pietsch, U.; Asawapirom, U.; Janietz, S.; Scherf, U.; Lieberwirth, I.; Wegner, G. *Macromolecules* **2006**, *39*, 2162–2171.
(12) Kline, R. J.; McGehee, M. D.; Kadnikova, E. N.; Liu, J.; Frechet, J. M. J.; Toney, M. F. *Macromolecules* **2005**, *38*, 3312–3319.
(13) Kline, R. J.; McGehee, M. D.; Kdnikova, E. N.; Liu, J.; Frechet, J. M. J. *Adv. Mater.* **2003**, *15*, 1519–1522.
(14) Zen, A.; Pflaum, J.; Hirschmann, S.; Zhuang, W.; Jaiser, F.; Asawapirom, U.; Rabe, J. P.; Scherf, U.; Neher, D. *Adv. Funct. Mater.* **2004**, *14*, 757–764.
(15) Merlo, J. A.; Frisbie, C. D. *J. Polym. Sci., Part B: Polym. Phys.* **2003**, *41*, 2674–2680.
(16) Gorjanc, T. C.; Levesque, I.; Lorio, M. D. *Appl. Phys. Lett.* **2004**, *84*, 930–932.
(17) Chang, J.; Sun, B.; Breiby, D. W; Nielsen, M. M.; Solling, T. I.; Giles, M.; McCulloch, I.; Sirringhaus, H. *Chem. Mater.* **2004**, *16*, 4772–4776.
(18) Kline, R. J.; McGehee, M. D.; Toney, M. F. *Nat. Mater.* **2006**, *5*, 222–228.
(19) Brinkmann, M.; Rannou, P. *Adv. Funct. Mater.* **2007**, *17*, 101–108.
(20) Zhang, R.; Li, B.; Iovu, C. M.; Jeffries-EL, M.; Sauve, G.; Cooper, J.; Jia, S.; Tristram-Nagle, S.; Smilgies, D. M.; Lambeth, D. N.; McCullough, R. D.; Kowalewski, T. *J. Am. Chem. Soc.* **2006**, *128*, 3480–3481.
(21) Tanase, C.; Meijer, E. J.; Blom, P. W. M.; de Leeuw, D. M. *Org. Electron.* **2003**, *4*, 33–37.
(22) Jia, H.; Srinivas, G.; Pant, G. K.; Wallace, R. M.; Gnade, B. E. *J. Vac. Sci. Technol. A* **2006**, *24*, 1228–1232.
(23) Loewe, R. S.; Khersonsky, S. M.; McCullough, R. D. *Adv. Mater.* **1999**, *11*, 250–253.
(24) Trznadel, M.; Pron, A.; Zagorska, M.; Chrzaszcz, R.; Pielichowski, J. *Macromolecules* **1998**, *31*, 5051–5058.
(25) Zen, A.; Neher, D.; Silmy, K.; Holländer, A.; Asawapirom, U.; Scherf, U. *Jpn. J. Appl. Phys.* **2005**, *44*, 3721–3727.
(26) Pietsch, U.; Holy, V.; Baumbach, T. *High-resolution X-ray Diffraction from Thin Films and Lateral Nanostructures*, 2nd ed.; Springer: Berlin, 2005; Vol. *2*, p 40.
(27) Yang, C.; Orfino, F. P.; Holdcroft, S. *Macromolecules* **1996**, *29*, 6510–6517.
(28) Tashiro, K.; Keiko, O.; Yasuhisa, M.; Masamichi, K.; Tsuyoshi, K.; Katsumi, Y. *J. Polym. Sci., Part B: Polym. Phys.* **1991**, *29*, 1223–1233.
(29) Prosa, T. J.; Winokur, M. J.; McCullough, R. D. *Macromolecules* **1996**, *29*, 3654–3656.
(30) Werzer, O.; Matoy, K.; Strohriegl, P.; Resel, R. *Thin Solid Films* **2007**, *515*, 5601–5605.
(31) Petermann, J.; Gleiter, H. *J. Polym. Sci.* **2003**, *14*, 555–558.
(32) Gennes, P. G.; Prost, J. *The Physics of Liquid Crystals*, 2nd ed.; Birman, S., Edwards, S. M., Eds.; Oxford University Press: New York, 1993; Vol. *10*, p 507.
(33) Meille, S. V.; Romita, V.; Caronna, T. *Macromolecules* **1997**, *30*, 7898–7905.

MA702802X